

Gravitational-wave sensitivity curves

C J Moore¹, R H Cole¹ & C P L Berry^{1,2}

¹ Institute of Astronomy, Madingley Road, Cambridge, CB3 0HA, United Kingdom

² School of Physics and Astronomy, University of Birmingham, Edgbaston, Birmingham B15 2TT, United Kingdom

E-mail: cjm96@ast.cam.ac.uk

Abstract. There are several common conventions use by the gravitational-wave community to describe the amplitude of sources and the sensitivity of detectors. These are frequently confused. We outline the merits of and differences between the various quantities used for parameterizing noise curves and characterizing gravitational-wave amplitudes. We conclude by producing plots that consistently compare different detectors. Similar figures can be generated on-line for general use at <http://www.ast.cam.ac.uk/~rhc26/sources/>.

PACS numbers: 04.30.-w, 04.30.Db, 04.80.Nn, 95.55.Ym

1. Introduction

The next few years promises to deliver the first direct detection of gravitational waves (GWs). This will most likely be achieved by the advanced Laser Interferometer Gravitational-wave Observatory (LIGO; Harry, 2010) and Virgo (Accadia et al., 2011) detectors operating in the frequency range ($10\text{--}10^3$) Hz. By the end of the decade, it is expected that pulsar timing arrays (PTAs; Foster & Backer, 1990) shall detect very low frequency GWs around 10^{-8} Hz. Further into the future, space-based detectors, such as the evolved Laser Interferometer Space Antenna (eLISA; Amaro-Seoane et al., 2012b), will probe GWs in the millihertz regime. These advances shall herald the beginning of multi-wavelength GW astronomy as a means of observing the Universe.

There already exists an extensive literature assessing the potential of all of these detectors to probe the astrophysics of various sources. There are several different methods commonly used to describe the sensitivity of a GW detector and the strength of a GW source. It is common practice to summarise this information on a sensitivity-curve plot. When producing these plots, it is desirable to have a consistent convention between detectors and sources which allows information about both to be plotted on the same graph. Ideally, the detectors and sources are represented in such a way that the relative detectability of the signals is immediately apparent from the plot.

In this work, we discuss the differing conventions commonly used in GW astronomy. The amplitude of a GW is a strain, a dimensionless quantity h . This gives a fractional change in length, or equivalently light travel time, across a detector. The strain is small, making it a challenge to measure: we are yet to obtain a direct detection of a GW. To calibrate our expectations for detection, it is necessary to quantify the sensitivity of our instruments and the strength of their target signals.

When discussing the loudness of sources and the sensitivity of detectors there are three commonly used parametrizations based upon the strain: the characteristic strain, the PSD and the spectral energy density. We aim to disambiguate these three and give a concrete comparison of different detectors. It is hoped that this will provide a useful reference for new and experienced researchers in this field alike.

We begin by expounding the various conventions and the relationships between the conventions in sections 2 and 3. A review of GW detectors (both current and proposed) is given in section 4 and a review of GW sources is given in section 5. In Appendix A several example sensitivity curves are presented. A website where similar figures can be generated is available at www.ast.cam.ac.uk/~rhc26/sources/. Here the user may select which sources and detectors to include to tailor the figure to their specific requirements.

2. Signal parametrization

2.1. Signal analysis preliminaries

Gravitational radiation has two independent polarization states denoted $+$ and \times ; a general signal can be described as a linear combination of the two polarization states, $h = A_+h_+ + A_\times h_\times$. The sensitivity of a detector to these depends upon the relative orientations of the source and detector. The output of a gravitational wave detector $s(t)$ contains a superposition of noise $n(t)$ and (possibly) the signal $h(t)$,

$$s(t) = n(t) + h(t) . \quad (1)$$

We shall work with the Fourier transform of the signal, using the conventions that

$$\tilde{x}(f) = \mathcal{F}\{x(t)\}(f) = \int_{-\infty}^{\infty} dt x(t) \exp(-2\pi i f t) , \quad (2)$$

$$x(t) = \mathcal{F}^{-1}\{\tilde{x}(f)\}(t) = \int_{-\infty}^{\infty} df \tilde{x}(f) \exp(2\pi i f t) . \quad (3)$$

For simplicity, it is assumed that the noise in the GW detector is stationary and Gaussian (with zero mean); under these assumptions the noise is fully characterised via the one-sided noise power spectral density (PSD) $S_n(f)$,

$$\langle \tilde{n}(f) \tilde{n}^*(f') \rangle = \frac{1}{2} \delta(f - f') S_n(f) , \quad (4)$$

where angle brackets $\langle \dots \rangle$ denote an ensemble average over many noise realisations (Cutler & Flanagan, 1994). In reality, we have only a single realisation to work with, however the ensemble average can be replaced by a time average for stationary stochastic noise. The procedure is to measure the noise over a sufficiently long duration T and then compute the Fourier transform $\tilde{n}(f)$ with a frequency resolution $\Delta f = T^{-1}$; this is repeated many times to give an average. The noise PSD $S_n(f)$ has units of inverse frequency.

Since the GW signal and detector output are both real it follows that $\tilde{h}(-f) = \tilde{h}^*(f)$ and $\tilde{n}(-f) = \tilde{n}^*(f)$; therefore, $S_n(f) = S_n(-f)$. The fact that $S_n(f)$ is an even function means that Fourier integrals over all frequencies can instead be written as integrals over positive frequencies only, e.g., (8) and (14); it is for this reason that $S_n(f)$ is called the *one-sided* PSD.[‡]

When integrated over all positive frequencies, the PSD gives the mean square noise amplitude. Starting by taking the time average of the square of the detector noise:

$$\begin{aligned} \overline{|n(t)|^2} &= \lim_{T \rightarrow \infty} \frac{1}{2T} \int_{-T}^T dt \, n(t) n^*(t) \\ &= \lim_{T \rightarrow \infty} \frac{1}{2T} \int_{-T}^T dt \int_{-\infty}^{\infty} df \int_{-\infty}^{\infty} df' \tilde{n}(f) \tilde{n}^*(f') \exp(2\pi i f t) \exp(-2\pi i f' t) \\ &= \lim_{T \rightarrow \infty} \frac{1}{2T} \int_{-T}^T dt \int_{-\infty}^{\infty} df \int_{-\infty}^{\infty} df' \mathcal{F}\{n(\tau)\}(f) [\mathcal{F}\{n(\tau)\}(f')]^* \\ &\quad \times \exp(2\pi i f t) \exp(-2\pi i f' t) , \end{aligned} \quad (5)$$

where we have substituted in using the definitions of the Fourier transform and its inverse. A property of Fourier transforms is that a time-domain translation by amount t is equivalent to a frequency-domain phase change $2\pi f t$; if $\mathcal{F}\{n(\tau)\}(f) = \tilde{n}(f)$, then $\mathcal{F}\{n(\tau - t)\}(f) = \tilde{n}(f) \exp(2\pi i f t)$. Therefore, the exponential factors in (5) may be absorbed as

$$\overline{|n(t)|^2} = \lim_{T \rightarrow \infty} \frac{1}{2T} \int_{-T}^T dt \int_{-\infty}^{\infty} df \int_{-\infty}^{\infty} df' \mathcal{F}\{n(\tau - t)\}(f) [\mathcal{F}\{n(\tau - t)\}(f')]^* . \quad (7)$$

Since the noise is a randomly varying signal, we can use the ergodic principle to equate a time average, denoted by $\overline{(\dots)}$, with an ensemble average, denoted by $\langle \dots \rangle$. The noise is stationary, consequently, its expectation value is unchanged by time-translation performed above. Therefore,

$$\overline{|n(t)|^2} = \int_{-\infty}^{\infty} df \int_{-\infty}^{\infty} df' \langle \tilde{n}(f) \tilde{n}^*(f') \rangle \quad (8)$$

$$\begin{aligned} &= \int_{-\infty}^{\infty} df \int_{-\infty}^{\infty} df' \frac{1}{2} S_n(f) \delta(f - f') \\ &= \int_0^{\infty} df \, S_n(f) , \end{aligned} \quad (9)$$

[‡] An alternative convention is to use the two-sided PSD $S_n^{(2)}(f) = S_n(f)/2$.

using (4).

Given a detector output, the challenge is to extract the signal. There is a well known solution to this problem which involves constructing a Wiener optimal filter (Wiener, 1949). Let $K(t)$ be the filter function with Fourier transform $\tilde{K}(f)$. Convolving this with the detector output gives a contribution from the signal and a contribution from the noise

$$(s * K)(\tau) = \int_{-\infty}^{\infty} dt [h(t) + n(t)] K(t - \tau) \approx \mathcal{S} + \mathcal{N}. \quad (10)$$

The signal contribution \mathcal{S} is defined as the expectation of the convolution in (10) when a signal is present, maximised by varying the offset to achieve the best overlap with the data. Since the expectation of pure noise is zero it, follows that

$$\mathcal{S} = \int_{-\infty}^{\infty} dt h(t) K(t) = \int_{-\infty}^{\infty} dt h(t) K^*(t) = \int_{-\infty}^{\infty} df \tilde{h}(f) \tilde{K}^*(f). \quad (11)$$

The squared contribution from noise \mathcal{N}^2 is defined as the mean square of the convolution in (10) when no signal is present,

$$\begin{aligned} \mathcal{N}^2 &= \int_{-\infty}^{\infty} dt \int_{-\infty}^{\infty} dt' K(t) K(t') \langle n(t) n(t') \rangle \\ &= \int_{-\infty}^{\infty} dt \int_{-\infty}^{\infty} dt' K(t) K^*(t') \int_{-\infty}^{\infty} df \int_{-\infty}^{\infty} df' \langle \tilde{n}(f) \tilde{n}^*(f') \rangle \exp[2\pi i(ft - f't')] \\ &= \int_{-\infty}^{\infty} df \frac{1}{2} S_n(f) \tilde{K}(f) \tilde{K}^*(f), \end{aligned} \quad (12)$$

using the definition of $S_n(f)$ from (4). Hence the signal-to-noise ratio (SNR) ϱ is given by

$$\varrho^2 = \frac{\mathcal{S}^2}{\mathcal{N}^2} = \frac{\left(\frac{1}{2} S_n(f) \tilde{K}(f) \middle| \tilde{h}(f) \right)^2}{\left(\frac{1}{2} S_n(f) \tilde{K}(f) \middle| \frac{1}{2} S_n(f) \tilde{K}(f) \right)}, \quad (13)$$

where we have introduced the inner product between signal \tilde{A} and \tilde{B} as (Finn, 1992)

$$\left(\tilde{A}(f) \middle| \tilde{B}(f) \right) = 4\Re \left\{ \int_0^{\infty} df \frac{\tilde{A}^*(f) \tilde{B}(f)}{S_n(f)} \right\}. \quad (14)$$

The optimum filter maximises the SNR in (13). From the Cauchy–Schwarz inequality, it follows that the optimum filter is

$$\tilde{K}(f) = \frac{\tilde{h}(f)}{S_n(f)}. \quad (15)$$

This is the Wiener filter, it may be multiplied by an arbitrary constant since this does not change the SNR. Using this form for $\tilde{K}(f)$, the squared SNR is

$$\varrho^2 = \int_0^{\infty} df \frac{4|\tilde{h}(f)|^2}{S_n(f)} = \left(\tilde{h}(f) \middle| \tilde{h}(f) \right). \quad (16)$$

In order to construct the Wiener filter, it is necessary to know *a priori* the form of the signal, $\tilde{h}(f)$.

Whilst the magnitude of the Fourier transform of the signal $|\tilde{h}(f)|$ provides a simple quantification of the GW amplitude as a function of frequency, it has one main deficiency. For an inspiralling source the instantaneous amplitude can be orders of magnitude below the noise level in the detector; however, as the signal continues over many orbits, the SNR can be integrated up to a detectable level. It is useful to have a quantification of the GW amplitude that accounts for this effect; three such methods are described in the following subsections.

2.2. Characteristic strain

The characteristic strain h_c is designed to include the effect of integrating an inspiralling signal. Its counterpart for describing noise is the noise amplitude h_n . These are defined as

$$h_c(f)^2 = 4f^2 \left| \tilde{h}(f) \right|^2, \quad (17)$$

$$h_n(f)^2 = f S_n(f), \quad (18)$$

such that the SNR in (16) may be written

$$\varrho^2 = \int_0^\infty d(\log f) \left[\frac{h_c(f)}{h_n(f)} \right]^2. \quad (19)$$

The strain amplitudes $h_c(f)$ and $h_n(f)$ are dimensionless. Using this convention, when plotting on a log–log scale, the area between the source and detector curves is related to the SNR via (19). This convention allows the reader to integrate by eye to assess the detectability of a given source (see figure A1).

An additional advantage of this convention is that the values on the strain axis for the detector curve $h_n(f)$ have a simple physical interpretation: they correspond to the root-mean-square noise in a bandwidth f . One downside to plotting characteristic strain is that the values on the strain axis $h_c(f)$ do not directly relate to the amplitude of the waves from the source. Another disadvantage is that the characteristic strain for a monochromatic source is infinite.

2.3. Power spectral density

A second commonly used quantity for sensitivity curves is the square root of the PSD (see figure A2). When discussing a detector this is

$$\sqrt{S_n(f)} = h_n(f) f^{-1/2}, \quad (20)$$

where we have used (18); by analogy, we can define an equivalent for source amplitudes

$$\sqrt{S_h(f)} = h_c(f) f^{-1/2} = 2f^{1/2} \left| \tilde{h}(f) \right|, \quad (21)$$

where we have used (17). Both $\sqrt{S_n(f)}$ and $\sqrt{S_h(f)}$ have units of $\text{Hz}^{-1/2}$. The root PSD is the most frequently plotted quantity in the literature.

The PSD has the nice property, demonstrated in (8), that integrated over all positive frequencies it gives the mean square amplitude of the signal in the detector. However, in one important regard it is less appealing than characteristic strain: the height of the source above the detector curve is no longer directly related to the SNR.

2.4. Energy density

A third way of describing the amplitude of a GW is through the energy carried by the waves. This has the advantage of having a clear physical significance. The energy density is most commonly used in sensitivity curves showing stochastic backgrounds of GWs (see section 3.2).

The energy in GWs is described by the Isaacson stress–energy tensor (Misner et al., 1973, section 35.15)

$$T_{\mu\nu} = \frac{c^2}{32\pi G} \langle \partial_\mu \bar{h}_{\alpha\beta} \partial_\nu \bar{h}^{\alpha\beta} \rangle , \quad (22)$$

where the angle brackets denote averaging over several wavelengths or periods. The energy density ρc^2 is given by the T_{00} component of this tensor. Consequently

$$\rho c^2 = \frac{c^2}{16\pi G} \int_{-\infty}^{\infty} df (2\pi f)^2 \tilde{h}(f) \tilde{h}^*(f) \quad (23)$$

$$= \int_0^{\infty} df \frac{\pi c^2}{4G} f^2 S_h(f) , \quad (24)$$

where the definition (21) have been used. Equation (23) gives the definition of the spectral energy density, the energy per unit volume of space, per unit frequency (Hellings & Downs, 1983)

$$S_E(f) = \frac{\pi c^2}{4G} f^2 S_h(f) ; \quad (25)$$

a corresponding expression for the noise can be formulated by replacing $S_h(f)$ with $S_n(f)$.

Cosmological studies often work in terms of the dimensionless quantity Ω_{GW} , the energy density per logarithmic frequency interval normalised to the critical density of the universe:

$$\Omega_{\text{GW}}(f) = \frac{f S_E(f)}{\rho_c c^2} . \quad (26)$$

The critical density of the universe is

$$\rho_c = \frac{3H_0^2}{8\pi G} , \quad (27)$$

where H_0 is the Hubble constant which is commonly parametrized as

$$H_0 = h_{100} \times 100 \text{ km s}^{-1} \text{ Mpc}^{-1}. \quad (28)$$

The reduced Hubble parameter h_{100} has nothing to do with strain. The most common quantity related to energy density to be plotted on sensitivity curves is $\Omega_{\text{GW}} h_{100}^2$ (figure A3) as this removes sensitivity to the measured value of the Hubble constant.

This quantity has one aesthetic advantage over the others: it automatically accounts for the fact that there is less energy in low frequency waves of the same amplitude. However, unlike characteristic strain, the area between the source and detector curves is no longer simply related to the SNR.

2.5. Relating the different descriptions

The dimensionless energy density in GWs Ω_{GW} , spectral energy density S_{E} , one-sided PSD, S_h , characteristic strain h_c and frequency-domain strain $\tilde{h}(f)$ are related via

$$H_0^2 \Omega_{\text{GW}}(f) = \frac{8\pi G}{3c^2} f S_{\text{E}}(f) = \frac{2\pi^2}{3} f^3 S_h(f) = \frac{2\pi^2}{3} f^2 h_c^2(f) = \frac{8\pi^2}{3} f^4 \left| \tilde{h}(f) \right|^2, \quad (29)$$

using (17), (21), (25), (26) and (27). Corresponding expressions for the noise are obtained by substituting $S_n(f)$ for $S_h(f)$, $h_n(f)$ for $h_c(f)$ and $\tilde{n}(f)$ for $\tilde{h}(f)$.

3. Types of source

GW signals can be broadly split into three categories: those from well-modelled sources, for which we have a description of the expected waveform; stochastic backgrounds, for which we can describe the statistical behaviour; and unmodelled (or poorly-modelled) transient sources. The classic example of a well-modelled source is the inspiral of two compact objects, this is discussed in section 3.1. Stochastic backgrounds can either be formed from many overlapping sources, which individually could be modelable, or from some intrinsically random process, these are discussed in section 3.2. An example of an unmodelled (or poorly-modelled) transient source is a supernova; searches for signals of this type are often called burst searches and are discussed in section 3.3.

3.1. Inspirals

Inspiralling binaries may be the most important GW source. They spend a variable amount of time in each frequency band. If ϕ is the orbital phase, then the number of cycles generated at frequency f can be estimated as

$$N_{\text{cycles}} = \frac{f}{2\pi} \frac{d\phi}{df} = \frac{f^2}{\dot{f}}, \quad (30)$$

where an overdot represents the time derivative and $\dot{\phi} = 2\pi f$. The squared SNR scales with N_{cycles} , so it would be expected that $h_c(f) \approx \sqrt{N_{\text{cycles}}} \tilde{h}(f)$.

The form for h_c can be derived from the Fourier transform in the stationary-phase approximation. Consider a source signal with approximately constant amplitude, h_0 , and central frequency f' . In this case,

$$h(t) = h_0 \exp[i\phi(t)] ; \quad (31)$$

$$\tilde{h}(f) = \int_{-\infty}^{\infty} dt h_0 \exp \left\{ 2\pi i \left[\frac{\phi(t)}{2\pi t} - f \right] t \right\} . \quad (32)$$

Without loss of generality, we can assume an initial phase of zero, such that $\phi(t) \approx 2\pi f' t$. The largest contribution to the integral comes from where the argument of the exponential is approximately zero. Expanding the exponent in powers of t about $f = f'$,

$$\begin{aligned} \tilde{h}(f) &\simeq \int_{-\infty}^{\infty} dt h_0 \exp \left[2\pi i \dot{f}' \left(t^2 + \frac{f' - f}{\dot{f}'} t \right) \right] \\ &\simeq h_0 \exp \left[-\pi i \frac{(f' - f)^2}{2\dot{f}'} \right] \int_{-\infty}^{\infty} dt \exp \left[2\pi i \dot{f}' \left(t + \frac{f' - f}{2\dot{f}'} \right)^2 \right] \\ &\simeq \frac{h_0}{\sqrt{2i\dot{f}'}} \exp \left[-\pi i \frac{(f' - f)^2}{2\dot{f}'} \right] . \end{aligned} \quad (33)$$

From (17) and (33), the characteristic strain for inspiralling sources is given by (Finn & Thorne, 2000)

$$h_c(f) = \sqrt{\frac{2f^2}{\dot{f}}} h_0 . \quad (34)$$

Equation (19) should be considered as the definition of characteristic strain and (34) a consequence of it for inspirals. Equation (34) is the relation between $h_c(f)$ and the instantaneous amplitude h_0 for an inspiralling source; for other types of source a new relation satisfying (19) has to be found.

3.2. Stochastic backgrounds

Another important source of GWs are stochastic backgrounds, which can be produced from a large population of unresolvable sources. These can be at cosmological distances, then it is necessary to distinguish the frequency in the source rest frame f_r from the measured frequency f ; the two are related through the redshift z via $f_r = (1 + z)f$.

The comoving number density of sources ν producing the background is also a function of redshift; if the sources producing the background are all in the local universe, then simply set $\nu(z) = \nu_0 \delta(z)$ and replace $d_L(z)$ with d in all that follows, where $d_L(z)$ and d are respectively the luminosity and comoving distances to the source, $d_L(z) = (1 + z)d$.

We shall assume the the individual sources are binaries, in which case the number density of sources is also be a function of component mass. It is convenient to work in terms of the chirp mass, defined as $\mathcal{M} = \mu^{3/5} M^{2/5}$, where μ is the reduced mass and M is the total mass of the binary. The comoving number density of sources shall be represented by $\nu(z, \mathcal{M})$.

Equation (26) gives an expression for the energy density in GWs per logarithmic frequency interval,

$$f S_E(f) = \frac{\pi c^2}{4G} f^2 h_c^2(f) . \quad (35)$$

The total energy emitted in the logarithmic frequency interval $d(\log f_r)$ by a single binary in the population is $[dE_{\text{GW}}/d(\log f_r)] d(\log f_r)$; the energy density may be written as

$$f S_E(f) = \int_0^\infty dz \frac{d\nu}{dz} \frac{1}{(1+z)} \frac{1}{d_L^2(z)} \frac{dE_{\text{GW}}}{d(\log f_r)} , \quad (36)$$

where the factor of $(1+z)^{-1}$ accounts for the redshift of the energy.

For simplicity, consider the background to comprise of binaries in circular orbits, with frequencies $f_{\text{GW}} = f_r/2$, which are far from their last stable orbit. The energy radiated may then be calculated using the quadrupole approximation (Peters & Mathews, 1963). The energy in GWs from a single binary per logarithmic frequency interval is,

$$\frac{dE_{\text{GW}}}{d(\log f_r)} = \frac{G^{2/3} \pi^{2/3}}{3} \mathcal{M}^{5/3} f_r^{2/3} , \quad (37)$$

between an minimum and maximum frequency set by the initial and final radius of the binary orbit. Here, we assume that the maximum and minimum frequencies are outside of the range of our detector and hence can be neglected. Using (35), (36) and (37), an expression for characteristic strain can now be found (Sesana et al., 2008)

$$h_c^2(f) = \frac{4G^{5/3}}{3\pi^{1/3}c^2} f^{-4/3} \int_0^\infty d\nu \int_0^\infty d\mathcal{M} \frac{d^2\nu}{dz d\mathcal{M}} \frac{1}{d_L^2(z)} \left(\frac{\mathcal{M}^5}{1+z} \right)^{1/3} . \quad (38)$$

From (38) it can be seen that the characteristic strain due to a stochastic background of binaries is a power law in frequency with spectral index $\alpha = -2/3$. The amplitude of the background depends on the population statistics of the binaries under consideration via $\nu(z, \mathcal{M})$. The power law is often parametrised as

$$h_c(f) = A \left(\frac{f}{f_0} \right)^\alpha , \quad (39)$$

and constraints are then placed on A . In practice, this power law also has upper and lower frequency cut-offs related to the population of source objects. A stochastic background from other sources, such as cosmic strings or relic GWs from the early Universe, can also be written in the same form as (39), but with different spectral indices: $\alpha = -7/6$ for cosmic strings or α in the range -1 to -0.8 for relic GWs (Jenet et al., 2006).

3.3. Burst sources

Some sources of GWs can produce signals with large amplitudes, greater than the detector noise. The typical duration of such a signal is short, of the order of a few wave periods, and so there is not time to accumulate SNR in each frequency band as for inspirals. As a consequence, waveform models are not required for detection; we simply rely on identifying the excess power produced by these burst sources. Typically, we may be looking for signals from core-collapse supernovae (Ott, 2009), the late stages of merging compact binaries, or more generally, signals from any unexpected or poorly modelled sources.

Burst searches are often carried out using time–frequency techniques. The data stream from a detector is temporally split into segments, the length of which can be tuned to give greater sensitivity to particular sources. Each segment is then transformed into the frequency domain, whitened and normalised to the noise spectrum to produce a time–frequency plot. Potential GW signals are identified by searching for clusters of pixels that contain an excess of power (e.g., Abadie et al., 2012a).

The presence of excess power across a number of pixels eliminates modelled noise sources, but such a cluster may also be caused by atypical noise within a detector. We can improve our confidence of a GW signal by making use of information obtained from other GW detectors. Signals across a network of detectors should have compatible arrival times (given the sky direction) as well as consistent amplitudes, frequencies and shapes of the waveform. Different pipelines are currently in use that analyse the signal consistency in different ways: both coincidence searches (Chatterji et al., 2004) and fully coherent methods (Klimenko et al., 2008) are used.

An important aspect of burst search algorithms is to accurately estimate the noise properties within each time segment. To this extent, null data streams can be constructed that are insensitive to real GW signals. In order to estimate the false alarm rate, the data from different detectors can be shifted in time to remove any genuine coincident GW signals. These time-shifts are then analysed to simulate the potential occurrence of coincident noise events. The algorithms are tuned using time-shifted data to ensure there is no bias in the final search.

As discussed in 3.1, the expected relation between $h_c(f)$ and a typical waveform $\tilde{h}(f)$ is

$$h_c(f) = \tilde{h}(f) \sqrt{N_{\text{cycles}}} , \quad (40)$$

where N_{cycles} is the number of cycles of radiation generated by the source. For bursts, N_{cycles} is of order unity and $\tilde{h}(f)$ is strongly peaked around some central frequency.

4. Detectors

In this section we introduce the detector noise curves used in Appendix A. We begin with a description of the basic operation of detectors. We then discuss ground-based detectors, space-based detectors and PTAs. The latter function somewhat different than conventional interferometers, so we include a brief introduction to PTA analysis. References for the noise curve used for individual detectors can be found in the relevant subsections, further information about the detectors can be discovered there.

4.1. Operating principle of an interferometric detector

All of the man-made detectors discussed in this section work on the principle of interferometry. Such detectors work by taking a beam of monochromatic light and splitting it into two beams travelling at some angle to each other. Each beam is passed in to an optical cavity where it undergoes a number of round trips before being recombined to form an interference pattern. The ends of the cavity are, in the ideal case, freely floating test masses which move in response to a passing GW, this effect is measured by observing the changing interference pattern.

The response of a detector to an incident plane-fronted GW depends upon the relative orientations of the detector and the incoming wave. Let us choose the origin of our coordinate system to be the beam-splitter of the interferometer, and l_1^i and l_2^i to be unit 3-vectors pointing along the two arms. In the absence of noise the output of the detector is the difference in strain between the two arms (Thorne, 1987)

$$h(t) = \frac{1}{2} h_{ij} (l_1^i l_1^j - l_2^i l_2^j) , \quad (41)$$

where h_{ij} are the spatial components of the GW metric perturbation. Let \hat{r}^i be the unit 3-vector pointing towards the source of the GWs, with spherical polar angles (θ, ϕ) relative to some axes fixed to the detector, and let p^i and q^i be unit vectors orthogonal to \hat{r}^i . We can now define the basis tensors

$$\begin{aligned} H_{ij}^+ &= p_i p_j - q_i q_j \\ H_{ij}^\times &= p_i q_j + q_i p_j . \end{aligned} \quad (42)$$

There remains a freedom in the coordinates described, a rotation of p^i and q^i through an angle ψ about \hat{r}^i known as the polarization angle. For a single frequency component, the strain induced by GW may be written as

$$h_{ij} = A_+ H_{ij}^+ \cos(2\pi f t) + A_\times H_{ij}^\times \cos(2\pi f t + \Delta\phi) , \quad (43)$$

where A_+ and A_\times are the amplitudes of the two polarisation states. Combining (41) and (43) allows the detector output to be written as

$$h(t) = F^+(\theta, \phi, \psi) A_+ \cos(2\pi f t) + F^\times(\theta, \phi, \psi) A_\times \cos(2\pi f t + \Delta\phi) , \quad (44)$$



Figure 1: The angular response function of an interferometric detector in (47) shown both as a surface plot and in an Aitoff–Hammer projection. The response is a function of two sky angles, θ and ϕ , and varies between 0 and 1. The two detector arms lie in the x – y plane either side of one of the zeros in the response.

where the response functions inherit their angular dependence from the choice of coordinates

$$F^+(\theta, \phi, \psi) = \frac{1}{2} H_{ij}^+ (l_1^i l_1^j - l_2^i l_2^j) , \quad (45)$$

$$F^\times(\theta, \phi, \psi) = \frac{1}{2} H_{ij}^\times (l_1^i l_1^j - l_2^i l_2^j) . \quad (46)$$

The response function of a two-arm interferometric detector is quadrupolar, an example is plotted in figure 1. Throughout this paper detector sensitivity refers to the polarisation and sky averaged sensitivity F , where

$$F^2 = \int_0^{2\pi} \frac{d\psi}{2\pi} \int_0^{2\pi} \frac{d\phi}{2\pi} \int_0^\pi \frac{\sin \theta d\theta}{2} \left[\frac{F^+(\theta, \phi, \psi)^2 + F^\times(\theta, \phi, \psi)^2}{2} \right] . \quad (47)$$

For a single 90° -interferometer, such as LIGO, the sky and polarisation averaged response is $F = \sqrt{1/5} \approx 0.447$.

A detector may consist of several interferometers. Let F_a be the averaged response of the a -th interferometer, the average response of a network of k detectors is obtained by adding in quadrature,

$$F_{\text{Total}}^2 = \frac{1}{k} \sum_{a=1}^k F_a^2 . \quad (48)$$

The averaging in (47) assumes a uniform distribution of polarisation angles ψ . This is the case for a stochastic background; however, for a non-inspiralling circular binary, the

polarisation is a function of the two spherical polar angles (ι, ξ) specifying the orientation of the binary’s orbital angular momentum. Here, ι is the inclination angle, the polar angle between the orbital angular momentum and the line joining the source to the detector $(-\hat{r})$ and ξ is the azimuthal angle around the same line. In this case, to characterise the detector sensitivity we average over all four angles $(\theta, \phi, \iota, \xi)$. If the binary is inspiralling, then the polarisation depends on still more parameters which need to be averaged over. These more complicated averages all have the property that they depend on both the detector and the source, hence they are unhelpful for our present purpose separating the source amplitude from the detector sensitivity. Additionally, the different averages do not work out to be so different from each other: Finn & Chernoff (1993) calculated the sensitivity for a detector with the LIGO geometry averaged over the four angles $(\theta, \phi, \iota, \xi)$ as $\sqrt{4/25} = 0.4$ times peak sensitivity, which should be compared with the value $\sqrt{1/5} \approx 0.447$ above. For the remainder of this paper the three-angle average defined in (47) is used.

4.2. Ground-based detectors

Ground-based detectors are the most numerous. A collection of interferometric detectors are listed in table 1, these are sensitive to GWs in the frequency range $\mathcal{O}(10\text{--}10^3)$ Hz. They all simulate free-floating test masses by suspending a mass from a pendulum system with natural frequency much greater than that of the GW. Their sensitivity curves include narrow lines that arise from noise sources in the instrument, including resonances in the suspension system and electrical noise at multiples of 60 Hz: these have been removed in the Appendix A figures for clarity. The detectors fall broadly into three categories: first-generation detectors, which have already operated; second-generation detectors currently under construction; and third-generation detectors at the planning stage.

The most notable ground-based detectors are LIGO and Virgo, which work in collaboration, supported by GEO600. LIGO and Virgo have completed science runs as first-generation detectors, now referred to as Initial LIGO (iLIGO) and Initial Virgo (iVirgo). They are currently being upgraded to second-generation detectors, advanced LIGO (aLIGO) and advanced Virgo (AdV). LIGO has two observatories: one at Hanford, Washington, which has two detectors; and another at Livingston, Louisiana. There is an agreement to move one of the upgraded Hanford detector systems to a location in India (Iyer et al., 2011; Unnikrishnan, 2013). The advanced detectors should start operation in the next couple of years, with LIGO-India following further in the future.

TAMA300 is a Japanese first-generation detector. Its successor is the Kamioka Gravitational Wave Detector (KAGRA), formerly the Large-scale Cryogenic Gravitational wave Telescope (LCGT), which is located underground in the Kamioka mine. It employs more sophisticated noise-reduction techniques than LIGO or Virgo, such as cryogenic cooling.

The Einstein Telescope (ET) is an ambitious proposal to construct an underground

Table 1: Summary of ground-based laser interferometers.

Detector	Country	Arm length	Approximate date	Generation
GEO600 ^a	Germany	600 m	2001–present	First
TAMA300 ^b	Japan	300 m	1995–present	First
iLIGO ^c	USA	4 km	2004–2010	First
Virgo ^d	Italy	3 km	2007–2010	First
aLIGO ^e	USA	4 km	<i>est.</i> 2015	Second
AdV ^f	Italy	3 km	<i>est.</i> 2016	Second
KAGRA ^g	Japan	3 km	<i>est.</i> 2018	Second
ET ^h	—	10 km	<i>est.</i> 2025	Third

^aGrote (2008), ^bAndo (2002), ^cAbbott et al. (2009), ^dAccadia et al. (2012),
^eHarry (2010), ^fAcernese et al. (2009), ^gSomiya (2012), ^hHild et al. (2011).

third-generation detector. Its location would provide shielding from seismic noise, allowing it to observe frequencies of 10–10⁴ Hz.

We use an interpolation to the data published on <https://wwwcascina.virgo.infn.it/advirgo/> (2013) for the AdV sensitivity curve, an interpolation to the data for version D of the KAGRA detector published on <http://gwcenter.icrr.u-tokyo.ac.jp/en/researcher/parameter> (2013) and analytic fits to the sensitivity curves from Sathyaprakash & Schutz (2009) for the remaining detectors.

4.3. Space-based detectors

Space-based detectors work on similar principles to ground based detectors, but with the test masses residing inside of independent, widely separated satellites. Space-based detectors are sensitive to lower frequency GWs than their ground-based counterparts; this is partly because space based detectors can have much longer arms, and partly because they are unaffected by seismic noise which limits the low frequency performance of ground-based detectors.

The canonical design for a space-based detector is the Laser Interferometer Space Antenna (LISA), which is sensitive to millihertz GWs. LISA would consist of three satellites flying in a triangular constellation with arms of length 5×10^9 m in a 1 AU orbit around the Sun, trailing the Earth by 20°. The laser arms in a LISA-like detector are not a cavity, the light only travels once along each arm. eLISA is a reduced version of LISA designed to probe the same frequency range, while proposals such as the Advanced Laser Interferometer Antenna (ALIA), Big Bang Observer (BBO) and Deci-hertz Interferometer GW Observatory (DECIGO) are designed to probe decihertz GWs.

4.3.1. LISA and eLISA The instrumental noise curves for LISA by the analytic fit given by Sathyaprakash & Schutz (2009), which we use for the plots in Appendix A. When observing individual sources with LISA there is an additional contribution to the noise from a background of unresolvable binaries. This is not included here as we consider the background as a source of GWs (see section 5.2.2). eLISA is a re-scoped version of the classic LISA mission, the main differences are shorter arms (10^9 m instead of 5×10^9 m), two laser arms instead of three, and a different orbit (drifting away from Earth instead of 20° Earth trailing). The effect of these changes is a slightly reduced peak sensitivity and a shift to higher frequencies. We use an analytic fit to the instrumental noise curve given by Amaro-Seoane et al. (2012a).

4.3.2. DECIGO, ALIA and BBO These missions are designed to probe the decihertz region of the GW spectrum; they are considerably more ambitious than the LISA or eLISA mission and their launches will be further into the future. We use a simple analytic fit to the sensitivity curve for ALIA (Bender et al., 2013), while for DECIGO and BBO, fits to the sensitivity curves given by Yagi & Seto (2011) are used.

4.4. Pulsar timing arrays (PTAs)

PTAs can be thought of as naturally occurring interferometers with galactic-scale arm lengths. Accordingly, they are sensitive to much lower frequencies than the detectors previously discussed. Each pulsar is a regular clock and the measured pulse arrival time can be compared against a prediction, leaving a residual which includes the effects of passing GWs. Using an array of these pulsars spread across the sky allows us to correlate residuals between different pulsars, to exploit the fact that GWs influence all pulsars whereas intrinsic pulsar noise does not. The correlation between different pulsars depends only on their angular separation on the sky, and has a distinctive shape, known as the Hellings and Downs curve (Hellings & Downs, 1983).

The redshift of the rate of arrival of pulses for a pulsar at a distance L from the Solar-System barycentre (SSB), in the direction of the unit spatial vector \hat{p} induced by a GW travelling in direction of the unit vector $\hat{\Omega}$ is (Anholm et al., 2009)

$$z(t, \hat{\Omega}) = \frac{1}{2} \frac{\hat{p}^j \hat{p}^i}{1 + \hat{\Omega} \cdot \hat{p}} \left[h_{ij}^{\text{Pulsar}} \left(t - \frac{L}{c}, \hat{\Omega} \right) - h_{ij}^{\text{Earth}}(t, \hat{\Omega}) \right] = \frac{1}{2} \frac{\hat{p}^j \hat{p}^i}{1 + \hat{\Omega} \cdot \hat{p}} \Delta h_{ij}(t, \hat{\Omega}) . \quad (49)$$

The redshift includes two terms: the pulsar term and the Earth term. The pulsar term is often neglected in PTA analysis as it can be considered as an extra noise term which averages to zero across the array. The experimentally measured quantity is not the redshift but the timing residual, the two are related via

$$R(t, \hat{\Omega}) = \int_0^t dt' z(t', \hat{\Omega}) . \quad (50)$$

All of the pulsars, and the Earth, are subject to the same metric perturbation field. This may be expressed in terms of its Fourier transform

$$h_{ij}(t, \vec{r}) = \sum_{A=+, \times} \int df \iint_{\mathbb{S}_2} d\hat{\Omega} \tilde{h}_A(f, \hat{\Omega}) e_{ij}^A(\hat{\Omega}) \exp \left[2\pi i f \left(t - \frac{\hat{\Omega} \cdot \vec{x}}{c} \right) \right], \quad (51)$$

where $e_{ij}^A(\hat{\Omega})$ is the A polarisation basis tensor for direction $\hat{\Omega}$ and \vec{r} is the spatial position. Choosing the SSB as the origin of our coordinate system, so the pulsar is at position $L\hat{p}$, gives

$$\Delta h_{ij}(t, \hat{\Omega}) = \sum_{A=+, \times} \int df \tilde{h}_A(f, \hat{\Omega}) e_{ij}^A(\hat{\Omega}) \exp(2\pi i f t) \left\{ \exp \left[-2\pi i f L \left(1 + \hat{p} \cdot \hat{\Omega} \right) \right] - 1 \right\}. \quad (52)$$

From (49) and (52), the Fourier transform of the redshift $\tilde{z}(f, \hat{\Omega})$ can be identified as

$$\tilde{z}(f, \hat{\Omega}) = \left\{ \exp \left[-2\pi i f L \left(1 + \hat{p} \cdot \hat{\Omega} \right) \right] - 1 \right\} \sum_{A=+, \times} \tilde{h}_A(f, \hat{\Omega}) F^A(\hat{\Omega}), \quad (53)$$

where

$$F^A(\hat{\Omega}) = \frac{e_{ij}^A(\hat{\Omega}) \hat{p}^j \hat{p}^i}{2 \left(1 + \hat{\Omega} \cdot \hat{p} \right)}. \quad (54)$$

The function $F^A(\hat{\Omega})$ may be regarded as the PTA equivalent of the detector response functions in (45). The stochastic background of GWs is fully characterised by the one-sided PSD via the expectation value

$$\left\langle \tilde{h}_A^*(f, \hat{\Omega}) \tilde{h}_{A'}(f', \hat{\Omega}') \right\rangle = \frac{1}{2} S_h(f) \delta^{(2)}(\hat{\Omega}, \hat{\Omega}') \delta_{AA'} \delta(f - f'), \quad (55)$$

where $\delta^{(2)}(\hat{\Omega}, \hat{\Omega}')$ is the delta-function on the sphere. From (53) and (55), the expectation of the product of signals from two different pulsars in directions \hat{p}_1 and \hat{p}_2 may be evaluated as

$$\langle \tilde{z}_1(f) \tilde{z}_2^*(f') \rangle = \frac{1}{2} S_h(f) \delta(f - f') \Gamma(f) \quad (56)$$

where,

$$\begin{aligned} \Gamma(f) = & \sum_{A=+, \times} \iint_{\mathbb{S}^2} d\hat{\Omega} \left\{ \exp \left[2\pi i f L_1 \left(1 + \hat{\Omega} \cdot \hat{p}_1 \right) \right] - 1 \right\} \\ & \times \left\{ \exp \left[-2\pi i f L_2 \left(1 + \hat{\Omega} \cdot \hat{p}_2 \right) \right] - 1 \right\} F_1^A(\hat{\Omega}) F_2^A(\hat{\Omega}). \end{aligned} \quad (57)$$

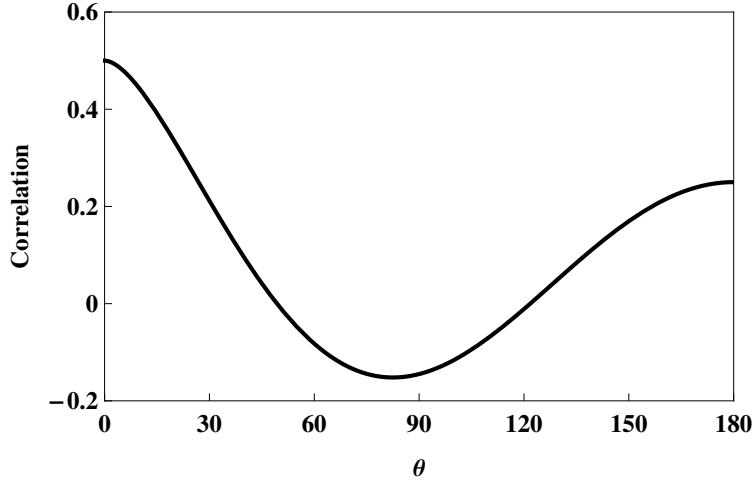


Figure 2: The Hellings & Downs (1983) curve, the correlation between two pulsars separated on the sky by an angle θ .

The overlap function $\Gamma(f)$ tends to a constant value in the limit that the distances to the pulsars are large compared to the wavelength of GWs; PTAs operate in this limit, so the overlap may be approximated as a constant,

$$\Gamma(f) \approx \Gamma_0 = \sum_{A=+, \times} \iint_{\mathbb{S}^2} d\hat{\Omega} F_1^A(\hat{\Omega}) F_2^A(\hat{\Omega}) . \quad (58)$$

Neglecting the exponential terms in the overlap is the frequency-domain equivalent of neglecting the pulsar term in (49). The integral may be evaluated to give an expression depending only on the angle θ between the two pulsars; this is the famous Hellings and Downs curve, shown in figure 2,

$$\Gamma_0 = \frac{1}{2} + \frac{3x}{2} \left(\ln x - \frac{1}{6} \right) \quad \text{where} \quad x = \frac{1 - \cos \theta}{2} . \quad (59)$$

The sensitivity bandwidth of a PTA is set by the sampling properties of the data set. If measurements are spaced in time by δt and taken for a total length of time T , then the PTA is sensitive to frequencies in the range $(1/T) < f < (1/\delta t)$. The characteristic strain that the PTA is sensitive to scales linearly with f in this range. This gives the wedge shaped curves plotted in Appendix A. The absolute value of the sensitivity is fixed by normalising to a calculated limit at a given frequency for each PTA. For a discussion of the sensitivities of PTA to both individual sources and stochastic background, see Moore et al. (2014).

There is a discrepancy between the treatment of PTA sensitivity curves here and the higher frequency detectors discussed in sections 4.2 and 4.3. When observing a long-lived source, such as an inspiral, with a high frequency detector the convention was to define a

characteristic strain to satisfy (19). Here the convention is to leave the strain untouched and instead adjust the PTA sensitivity curve with observation time, again to satisfy (19). This discrepancy is an unfortunate result of the conventions in use by the different GW communities; however, it is also natural given the sources under observation. When observing a transient source, such as a burst or inspiral, which changes within the lifetime of the detector, it is natural to consider the detector as performing constantly while the signal changes. However, when observing a monochromatic source or a stochastic background, which is unchanging over the detector lifetime, it is more natural to consider the source as being fixed and the sensitivity of the detector gradually improving. All that is required by the definition in (19) is that the ratio $h_c(f)/h_n(f)$ is constant.

4.4.1. Current PTAs The PTAs currently in operation are the European Pulsar Timing Array (EPTA§, Kramer & Champion (2013)), the Parkes Pulsar Timing Array (PPTA|| Hobbs (2013)) based in Australia, and the North American Nanohertz Observatory for Gravitational waves (NANOGrav¶ McLaughlin (2013)). There are published limits on the amplitude of the stochastic background from all three detectors: the most recent from EPTA is van Haasteren et al. (2011), from PPTA is Shannon et al. (2013) and from NANOGrav is Arzoumanian et al. (2014). These are all comparable and we use the EPTA limits in Appendix A, the figures show the published limit based on an analysis of five pulsars over approximately ten years.

4.4.2. The International Pulsar Timing Array Combining the existing arrays would yield a single PTA using approximately 4 times as many pulsars; this consortium of consortia is known as the International Pulsar Timing Array (IPTA⁺ Manchester & IPTA (2013)). The IPTA curves plotted in the figures are based on 20 pulsars timed for twice as long as the current EPTA.

4.4.3. SKA The next great advancement in radio astronomy shall come with the completion of the Square Kilometre Array (SKA; Dewdney et al., 2009). This shall greatly increasing the sensitivity of pulsar timing (Kramer et al., 2004). The sensitivity curves plotted in Appendix A for the SKA assumes an rms error on the timing residuals a factor of 10 better than current PTAs, and 20 pulsars timed for twice as long as the current EPTA.

§ <http://www.epta.eu.org/>

|| <http://www.atnf.csiro.au/research/pulsar/ppta/>

¶ <http://nanograv.org/>

⁺ <http://www.ipta4gw.org/>

5. Astrophysical sources

All the sources described here are represented by shaded boxes in Appendix A. The boxes are drawn in such a way that there is a reasonable event rate for sources at a detectable SNR. Descriptions of each source are given in the following sections. Sources with short durations (i.e., burst sources) and sources which evolve in time over much longer timescales than our observations are drawn with flat-topped boxes for $h_c(f)$. Inspiralling binaries, or stochastic backgrounds of binaries, are drawn with a sloping top proportional to $f^{-2/3}$ for $h_c(f)$, which is result derived in section 3.2. The width of the box gives the range of frequencies sources of a given type can have a while remaining at a detectable amplitude.

5.1. Sources for ground based detectors

5.1.1. Neutron star binaries The inspiral and merger of a pair of neutron stars is the primary target for ground based detectors. The expected event rate for this type of source is uncertain, but estimates centre around $\rho_{\text{NS-NS}} = 1.3 \times 10^{-4} \text{ Mpc}^{-3} \text{ yr}^{-1}$ (Abadie et al., 2012b). Plotted in Appendix A is a box with an amplitude such that it produces a ratio $h_c/h_n = 16$ for Advanced LIGO at peak sensitivity and a width between (3–300) Hz.

5.1.2. Supernovae Simulations of core-collapse supernovae show that GWs between (10^2 – 10^3) Hz can be produced (Kotake et al., 2006). The GW signal undergoes $\mathcal{O}(1)$ oscillation and is hence burst-like. Dimmelmeyer et al. (2002) calculate the average maximum amplitude of GWs for a supernova at distance r as

$$h = 8.9 \times 10^{-21} \left(\frac{10 \text{ kpc}}{r} \right). \quad (60)$$

The event rate for supernovae is approximately $\rho_{\text{SN}} = 5 \times 10^{-4} \text{ Mpc}^{-3} \text{ yr}^{-1}$. The boxes plotted in Appendix A correspond to a distance $r = 300 \text{ kpc}$ with the frequency range quoted above. The LIGO and Virgo detectors have already placed bounds on the event rate for these sources (Abadie et al., 2012a).

5.1.3. Continuous waves from rotating neutron stars Rotating neutron stars are a source of continuous GWs if they possess some degree of axial asymmetry (Abbott et al., 2007; Prix, 2009; Aasi et al., 2013). The signals are near monochromatic with a frequency twice the rotation frequency of the neutron star, and are a potential source for ground-based detectors. The amplitude of the GWs depends upon the deformation of the neutron star, which itself depends upon the neutron star equation of state. This is currently uncertain (Lattimer, 2012). Several known pulsars could be sources for the advanced detectors and upper limits from the initial detectors help to constrain the deformations. The boxes plotted in Appendix

A correspond to the upper limits placed on a GW signal from the Crab pulsar (Aasi et al., 2014b), extrapolated across a frequency range between $(20\text{--}10^3)$ Hz.

5.2. Sources for space based detectors

For a review of the GW sources for space based missions see, for example, Amaro-Seoane et al. (2012a), Gair et al. (2012) or Jennrich et al. (2011).

5.2.1. Massive black hole binaries Space-based detectors shall be sensitive to equal-mass mergers in the range $(10^4\text{--}10^7) M_\odot$. Predictions of the event rate for these mergers range from $\mathcal{O}(10\text{--}100)$ yr $^{-1}$ for eLISA with SNRs of up to 10^3 (Seoane et al., 2013). The large range in the rate reflects our uncertainty in the growth mechanisms of the supermassive black hole population (Volonteri, 2010). Plotted in Appendix A are boxes with a ratio $h_c/h_n = 100$ for eLISA at its peak sensitivity. The range of frequencies plotted is $(3 \times 10^{-4}\text{--}3 \times 10^{-1})$ Hz, this corresponds to circular binaries in the mass range quoted above.

5.2.2. Galactic white dwarf binaries For space-based detectors, these are the most numerous GW sources; they are also the only guaranteed source since several detectable systems (known as verification binaries) have already been identified by electromagnetic observations (Stroeer & Vecchio, 2006).

Galactic binaries divide into two classes: the unresolvable and the resolvable galactic binaries. The unresolvable binaries overlap to form a stochastic background as discussed in section 3.2. The distinction between resolvable and unresolvable is detector specific; here we choose LISA. This boundary will not be too different for eLISA but would move substantially for either of the decihertz detectors. Plotted in Appendix A is the estimate of this background due to Nelemans et al. (2001) where an observation time of one year has been assumed,

$$h_c(f) = 5 \times 10^{-21} \left(\frac{f}{10^{-3} \text{ Hz}} \right)^{-2/3}. \quad (61)$$

Estimates for the event rate of resolvable binaries centre around $\mathcal{O}(10^3)$ events for eLISA. The boxes plotted in Appendix A have a ratio $h_c/h_n = 50$ for eLISA at its peak sensitivity. The frequency range of the box is $(3 \times 10^{-4}\text{--}10^{-2})$ Hz, estimated from Monte Carlo population simulation results presented in Amaro-Seoane et al. (2012a).

5.2.3. Extreme mass-ratio inspirals EMRIs occur when a compact stellar mass object inspirals into a supermassive black hole. There is extreme uncertainty in the event rate for EMRIs due to the poorly constrained astrophysics in galactic centres (e.g., Merritt et al., 2011); the best guess estimate is around 25 events per year with eLISA with $\text{SNR} \geq 20$ (Seoane et al., 2013). The boxes plotted in Appendix A have a characteristic strain of

$h_c = 3 \times 10^{-20}$ at 10^{-2} Hz, which corresponds to a $10M_\odot$ BH inspiralling into a 10^6M_\odot black hole at a luminosity distance of 1 Gpc. The frequency width of the box is somewhat unknown; EMRI events can occur into a black hole of any mass, and hence EMRIs can, in principal, occur at any frequency, so the boxes in Appendix A are drawn with a width comparable to that of the LISA sensitivity curve.

5.3. Sources for PTAs

5.3.1. Supermassive black hole binaries The main target for PTAs is a stochastic background of GWs produced by a population of supermassive black hole binaries at cosmological distances (Sesana et al., 2008). Supermassive black holes are known to lie at the centres of most galaxies and the black hole mergers are associated with the mergers of the host galaxies (Volonteri et al., 2003; Ferrarese & Ford, 2005). The current best published limit for the amplitude of the stochastic background is $h_c = 6 \times 10^{-15}$ at a frequency of $f_0 = 1 \text{ yr}^{-1}$ (van Haasteren et al., 2011). There is strong theoretical evidence that the actual background lies close to the current limit (Sesana, 2012).

Supermassive black hole binaries at higher frequencies are inspiralling faster and hence there are fewer of them per frequency bin. At a certain frequency, these sources will cease to be a background and become individually resolvable. It is currently unclear whether PTAs will detect an individual binary or a stochastic background first. Plotted in Appendix A for the unresolvable background is a third of the current limit with a cut off frequency of $f = 1 \text{ yr}^{-1}$ which is suggested by Monte Carlo population studies (Sesana et al., 2008). For the resolvable sources the amplitude of the current limit is plotted between $(3 \times 10^{-9} - 3 \times 10^{-7})$ Hz.

5.4. Cosmological sources

In addition to the sources above, early Universe processes, such as inflation (Grishchuk, 2005) or a first-order phase transition (Binétruy et al., 2012), could have created GWs. More speculatively, it has been hypothesised that cosmic strings could also be a potential source (Damour & Vilenkin, 2005; Binétruy et al., 2012; Aasi et al., 2014a). These relic GWs allow us to explore energy scales far beyond those accessible by other means, providing insight into new and exotic physics. The excitement surrounding the tentative discovery by BICEP2 of the imprint of primordial GWs (generated during inflation) in the cosmic microwave background (Ade et al., 2014), and the subsequent flurry of activity, has shown the scientific potential of such cosmological GWs. These GW signals are so alluring because they probe unknown physics; this also makes them difficult to predict. Cosmological stochastic backgrounds have been predicted across a range of frequencies with considerable variation in amplitude. As a consequence of this uncertainty, although we could learn much from measuring these signals, we have not included them amongst the sources shown in Appendix

A.

6. Concluding remarks

When quantifying the sensitivity of a GW detector and the loudness of a GW source, there are three commonly used quantities: the characteristic strain, the power spectral density, and the spectral energy density. We have carefully defined these quantities and derived the relationships between them. The characteristic strain (section 2.2) is most directly related to the SNR, the PSD is mostly closely related to the mean square amplitude in the detector, and the energy density has a clear physical interpretation. We have produced example plots using each of these quantities for a wide range of detectors and sources. The predicted source amplitudes are based on astrophysical estimates of the event rates and are subject to varying degrees of uncertainty.* Interactive versions of these plots, with user-specified detectors and sources, are available on-line at <http://www.ast.cam.ac.uk/~rhc26/sources/>. Trying to summarise an entire field of astronomy on one plot is an impossible task; however, we hope that the figures and analysis presented here provide useful insight.

Acknowledgments

CJM, RHC and CPLB are supported by the Science & Technology Facilities Council. We are indebted to Jonathan Gair, for useful advice and proof-reading the manuscript. We also thank Stephen Taylor and Justin Ellis for useful conversations about pulsar timing.

Appendix A. Sensitivity curves

The plots in this section show all of the detectors and sources described in the main text. Clearer, interactive versions of these plots, allowing for removal of any of the curves, may be created and downloaded on-line, <http://www.ast.cam.ac.uk/~rhc26/sources/>. The detector noise curves all have their resonance spikes removed for clarity.

References

- Aasi, J., Abadie, J., Abbott, B. P., et al. 2013, prd, 87, 042001
- Aasi, J., Abadie, J., Abbott, B. P., et al. 2014a, Physical Review Letters, 112, 131101
- . 2014b, The Astrophysical Journal, 785, 119(18)
- Abadie, J., Abbott, B. P., Abbott, R., et al. 2012a, prd, 85, 122007
- . 2012b, prd, 85, 082002

* There is also the exciting possibility of sources yet to be considered.

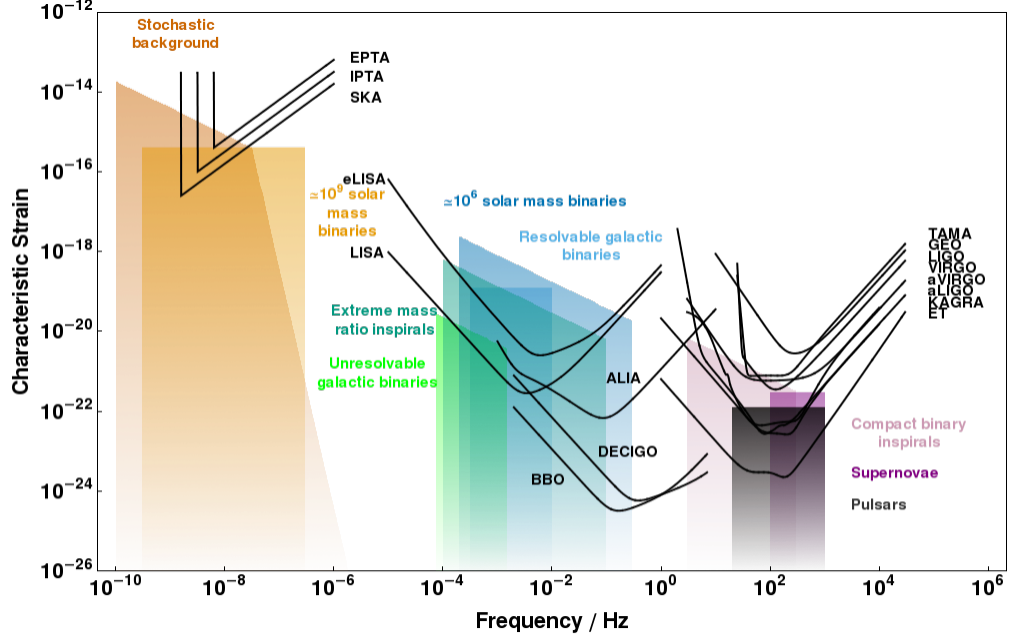


Figure A1: A plot of characteristic strain against frequency for a variety of detectors and sources.

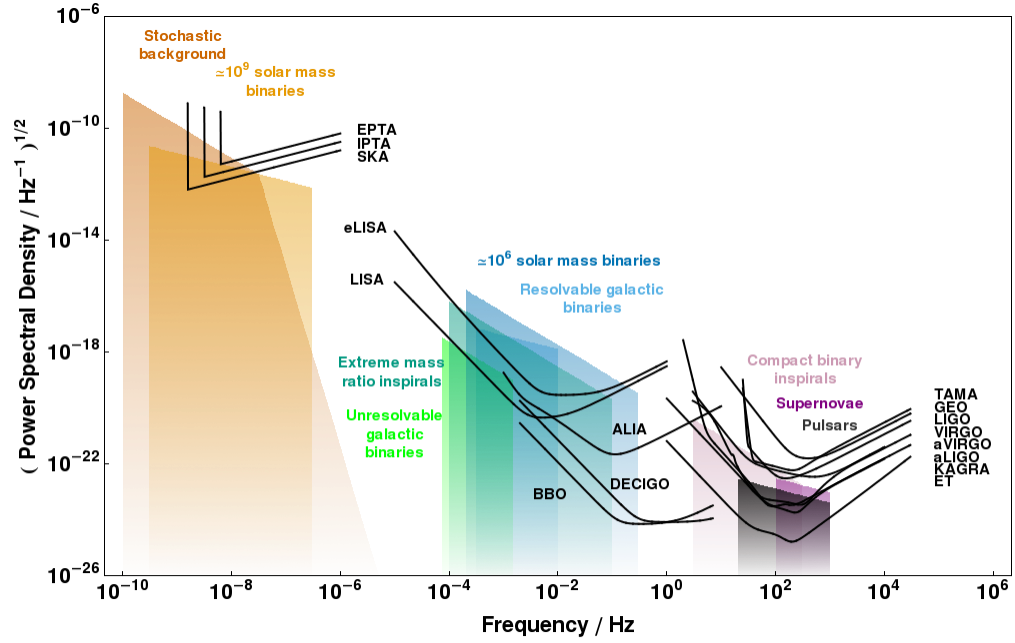


Figure A2: A plot of the square root of power spectral density against frequency for a variety of detectors and sources.

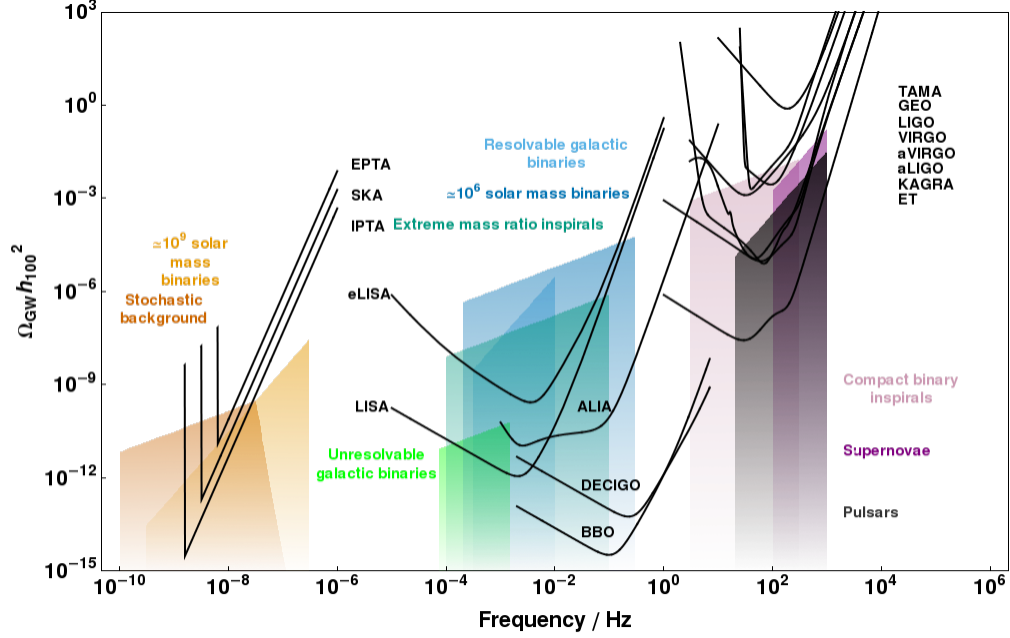


Figure A3: A plot of the dimensionless energy density in GWs against frequency for a variety of detectors and sources.

- Abbott, B., Abbott, R., Adhikari, R., et al. 2007, Physical Review D, 76, 082001
- Abbott, B. P., Abbott, R., Adhikari, R., et al. 2009, Reports on Progress in Physics, 72, 076901
- Accadia, T., Acernese, F., Antonucci, F., et al. 2011, Classical and Quantum Gravity, 28, 114002
- Accadia, T., Acernese, F., Alshourbagy, M., et al. 2012, Journal of Instrumentation, 7, 03012
- Acernese, F., et al. 2009, Advanced Virgo Baseline Design, Virgo Technical Report VIR-0027A-09
- Ade, P. A. R., Aikin, R. W., Barkats, D., et al. 2014, Physical Review Letters, 112, 241101
- Amaro-Seoane, P., Aoudia, S., Babak, S., et al. 2012a, ArXiv e-prints, arXiv:1201.3621
- . 2012b, cqg, 29, 124016
- Ando, M. 2002, Classical and Quantum Gravity, 19, 1409
- Anholm, M., Ballmer, S., Creighton, J. D. E., Price, L. R., & Siemens, X. 2009, prd, 79, 084030
- Arzoumanian, Z., Brazier, A., Burke-Spolaor, S., et al. 2014, 21
- Bender, P. L., Begelman, M. C., & Gair, J. R. 2013, Classical and Quantum Gravity, 30, 165017

- Binétruy, P., Bohé, A., Caprini, C., & Dufaux, J.-F. 2012, *Journal of Cosmology and Astroparticle Physics*, 2012, 027
- Chatterji, S., Blackburn, L., Martin, G., & Katsavounidis, E. 2004, *Classical and Quantum Gravity*, 21, S1809
- Cutler, C., & Flanagan, É. E. 1994, *Physical Review D*, 49, 2658
- Damour, T., & Vilenkin, A. 2005, *Physical Review D*, 71, 063510
- Dewdney, P. E., Hall, P. J., Schilizzi, R. T., & Lazio, T. J. L. W. 2009, *Proceedings of the IEEE*, 97, 1482
- Dimmelmeier, H., Font, J. A., & Müller, E. 2002, *Å*, 393, 523
- Ferrarese, L., & Ford, H. 2005, *Space Science Reviews*, 116, 523
- Finn, L. S. 1992, *Physical Review D*, 46, 5236
- Finn, L. S., & Chernoff, D. F. 1993, *prd*, 47, 2198
- Finn, L. S., & Thorne, K. S. 2000, *prd*, 62, 124021
- Foster, R. S., & Backer, D. C. 1990, *apj*, 361, 300
- Gair, J. R., Vallisneri, M., Larson, S. L., & Baker, J. G. 2012, *ArXiv e-prints*, arXiv:1212.5575
- Grishchuk, L. P. 2005, *Physics-Uspekhi*, 48, 1235
- Grote, H. 2008, *Classical and Quantum Gravity*, 25, 114043
- Harry, G. M. 2010, *Classical and Quantum Gravity*, 27, 084006
- Hellings, R. W., & Downs, G. S. 1983, *apjl*, 265, L39
- Hild, S., Abernathy, M., Acernese, F., et al. 2011, *Classical and Quantum Gravity*, 28, 094013
- Hobbs, G. 2013, *Classical and Quantum Gravity*, 30, 224007
- Iyer, B., et al. 2011, *LIGO-India, Proposal of the Consortium for Indian Initiative in Gravitational-wave Observations (IndIGO)*, Tech. Rep. M1100296
- Jenet, F. A., Hobbs, G. B., van Straten, W., et al. 2006, *apj*, 653, 1571
- Jennrich, O., Binétruy, P., Colpi, M., et al. 2011, *NGO Revealing a hidden Universe: opening a new chapter of discovery*, Tech. Rep. ESA/SRE(2011)19, European Space Agency, Noordwijk
- Klimenko, S., Yakushin, I., Mercer, A., & Mitselmakher, G. 2008, *Classical and Quantum Gravity*, 25, 114029
- Kotake, K., Sato, K., & Takahashi, K. 2006, *Reports on Progress in Physics*, 69, 971
- Kramer, M., Backer, D. C., Cordes, J. M., et al. 2004, *New Astronomy Reviews*, 48, 993
- Kramer, M., & Champion, D. J. 2013, *Classical and Quantum Gravity*, 30, 224009
- Lattimer, J. M. 2012, *Annual Review of Nuclear and Particle Science*, 62, 485

- Manchester, R. N., & IPTA. 2013, *Classical and Quantum Gravity*, 30, 224010
- McLaughlin, M. A. 2013, *Classical and Quantum Gravity*, 30, 224008
- Merritt, D., Alexander, T., Mikkola, S., & Will, C. M. 2011, *Physical Review D*, 84, 044024
- Misner, C. W., Thorne, K. S., & Wheeler, J. A. 1973, *Gravitation*
- Moore, C. J., Taylor, S. R., & Gair, J. R. 2014, ArXiv e-prints, arXiv:1406.5199
- Nelemans, G., Yungelson, L. R., & Portegies Zwart, S. F. 2001, *Astron. Astrophys.*, 375, 890
- Ott, C. D. 2009, *Classical and Quantum Gravity*, 26, 063001
- Peters, P. C., & Mathews, J. 1963, *Physical Review*, 131, 435
- Prix, R. 2009, in *Neutron Stars and Pulsars*, ed. W. Becker, *Astrophysics and Space Science Library* (Berlin: Springer), 651–685
- Sathyaprakash, B. S., & Schutz, B. F. 2009, *Living Reviews in Relativity*, 12, 2
- Seoane, P. A., Aoudia, S., Audley, H., et al. 2013, ArXiv e-prints, arXiv:1305.5720
- Sesana, A. 2012, ArXiv e-prints, arXiv:1211.5375
- Sesana, A., Vecchio, A., & Colacino, C. N. 2008, *mn*, 390, 192
- Shannon, R. M., Ravi, V., Coles, W. A., et al. 2013, *Science*, 342, 334
- Somiya, K. 2012, *Classical and Quantum Gravity*, 29, 124007
- Stroeer, A., & Vecchio, A. 2006, *Classical and Quantum Gravity*, 23, 809
- Thorne, K. S. 1987, in *Three Hundred Years of Gravitation*, ed. S. W. Hawking & W. Israel (Cambridge: Cambridge University Press), 330–458
- Unnikrishnan, C. S. 2013, *International Journal of Modern Physics D*, 22, 1341010
- van Haasteren, R., Levin, Y., Janssen, G. H., et al. 2011, *mn*, 414, 3117
- Volonteri, M. 2010, *The Astronomy and Astrophysics Review*, 18, 279
- Volonteri, M., Haardt, F., & Madau, P. 2003, *The Astrophysical Journal*, 582, 559
- Wiener, N. 1949, *The extrapolation, interpolation and smoothing of stationary time series* (The M.I.T. Press)
- Yagi, K., & Seto, N. 2011, *prd*, 83, 044011